Automatic Power Frequency Rejection Instrumentation for Nonintrusive Frequency Signature Tracking

Kahyun Lee, *Member, IEEE*, Lukasz Huchel, *Student Member, IEEE*, Daisy H. Green, *Graduate Student Member, IEEE*, and Steven B. Leeb, *Fellow, IEEE*

***Abstract*— This article presents a design for data acquisition hardware that can automatically track and reject utility frequency components of a measured current or voltage waveform. Measurements of subtle harmonic content in the waveform can therefore be made with the full dynamic range of the on-board analog-to-digital converter. This permits the detection of small, higher frequency signals for applications to condition-based maintenance and energy scorekeeping. Experimental demonstrations in this article show the hardware prototype isolating the rotor slot harmonics in a motor's input current. The high-resolution measurements of slot harmonics permit the estimation of motor speed from the detected slot harmonic frequency and the rejected fundamental frequency. The performance and accuracy of the speed estimator are demonstrated with both steady-state and transient experiments.**

***Index Terms*— Frequency tracking, nonintrusive monitoring, rotor slot harmonic, speed estimation, switched-capacitor (SC) notch filter.**

I. Introduction

VALUABLE information for diagnostics, control, and energy-scorekeeping may be found over a range of frequencies and amplitudes in utility waveforms. The ac utility effectively creates a substantial "carrier frequency" component at the utility frequency that indicates real and reactive power demand. Other frequency content, for example, in the current waveforms demanded by a load, can serve as important tell-tale signatures for identifying loads and recognizing operating state and fault conditions. This additional frequency content may be at harmonic multiples of the utility frequency, or distributed in other ways, for example, as a multiple or function of both utility frequency and slip frequency in a motor. The relative amplitude of signals like current at the utility frequency versus motor slot harmonic frequencies may vary over several orders of magnitude [1]. This creates a significant practical problem in achieving an adequate dynamic range to observe all signals of interest. The problem is compounded by normal variations in the utility frequency, which complicates the design of data acquisition instrumentation for making complete measurements of interest.

This article presents a custom design for data acquisition hardware that can automatically track and reject "carrier (utility) frequency" content in a nonintrusive current measurement, permitting the resolution of subtle higher harmonic content with the full dynamic range of an available analog-to-digital converter (ADC). This new instrumentation design automatically tracks variations in utility frequency and adapts to ensure reliable measurements of relatively small signals which are present in the waveform of interest.

Knowledge of shaft speed, for example, assists with many control and monitoring applications for electric machines [2]–[7]. Using invasive approaches for speed estimation adds sensors to machines, adding complexity and cost [2]–[4]. Installation of the sensors, cables for power and communication, and interface circuits requires additional work and space. These approaches are also vulnerable to faults in each component [6]. Noninvasive, speed sensorless monitoring can reliably estimate speed [6]–[15] with varying approaches and effort. Commonly used estimation methods require detailed motor models [8]–[10] with accurate parameter estimates [10], [11]. Machine saliencies [12], [13] and magnetic variations [14], [15] allow for speed estimation without dedicated speed sensors or a detailed machine model. These signals create tell-tale signs at frequencies higher than the utility, which can be examined.

However, three problems challenge efforts to implement practical nonintrusive speed sensors for electric machines. First, slot harmonic signals are much smaller in size and located in higher frequency bands when compared with the fundamental component of current. Notch filters have been applied to attenuate the line frequency component and amplify high-frequency harmonics [1], [16]. Subtle variations in the utility frequency can defeat the efficacy of this approach as utility waveforms slide out of the stopband of a tightly tuned filter. Second, as shaft speed changes with mechanical load, the slot harmonic frequencies change with changing machine slip. Complex circuit solutions can phase-lock to these changes [17]–[19], but digital signal processing methods permit more flexible implementations assuming a reliable

Manuscript received April 24, 2020; accepted June 24, 2020. Date of publication July 29, 2020; date of current version November 23, 2020. The Associate Editor coordinating the review process was Dr. Fabricio Guimaraes Baptista. *(Corresponding author: Kahyun Lee.)*

The authors are with the Department of Electrical Engineering and Computer Science (EECS), Massachusetts Institute of Technology, Cambridge, MA 02139 USA (e-mail: khylee@mit.edu; lhuchel@mit.edu; dhgreen@mit.edu; sbleeb@mit.edu).

Digital Object Identifier 10.1109/TIM.2020.3009339

measurement of slot harmonics can be made [20]–[22]. Third, because an electric machine typically generates a family of harmonics, tracking applications can become confused by coincident changes in utility frequency and higher harmonic, for example, slip-related frequency [1], [15], [22], [23].

This article also presents a nonintrusive speed estimation method using the proposed tracking hardware and demonstrates the speed estimation performance with induction motors as a working example. The data acquisition board with an automatically tunable notch filter tracks utility frequency and provides high resolution measurements of higher harmonics as the utility frequency experiences inevitable variations. To detect key slot harmonics from the filtered data, a slot harmonic tracking algorithm is proposed. It includes an optimization process to increase the accuracy of frequency detection and improve dynamic performance. Reliable harmonic tracking is achieved as the motor load varies by taking advantage of the inherent slip range typically observed for efficient operation in most induction machines. The accuracy and dynamic performance of the proposed speed estimation techniques are verified through experiments at various operating conditions and are used to demonstrate the utility of the proposed instrumentation and harmonic tracking algorithm for enhanced nonintrusive load monitoring.

II. Frequency Signatures

Most impedance loads draw current signatures with frequency content beyond the utility frequency. Induction motors, an industry workhorse, for example, have rotor slots that create harmonics in phase currents, voltages, and machine fluxes [1], [16]. These harmonics can be measured in the air-gap flux, stator current, and stator voltage at frequencies

$$f_{\mathrm{h}} = f_{\mathrm{s}}\left[(kR + n_{\mathrm{d}})\frac{1-s}{p} + v\right] \tag{1}$$

where f_{s} is the supply frequency, $k = 0, 1, 2, \ldots$ is the order of rotor slot harmonics, R is number of rotor slots, p is the number of pole pairs, $n_{\mathrm{d}} = 0, \pm 1, \ldots$ is the order of rotor eccentricity or decentering as it rotates with respect to the stator, s is the rotor slip, and $v = \pm 1, \pm 3, \ldots$ is the order of stator MMF harmonics [12]. If the motor is mechanically healthy ($n_{\mathrm{d}} = 0$) and fed with a pure sinusoidal supply ($v = 1$), the harmonic content in the line current demanded by the machine can be expected to distribute around a simplified set of slot harmonic frequencies that may be well represented or tracked by following the "principal slot harmonic" (PSH) at $k = 1$, expressed as follows:

$$f_{\mathrm{PSH}} = f_{\mathrm{s}}\left[\frac{R}{p}(1-s) + 1\right]. \tag{2}$$

Fig. 1 shows a measured example of the current spectrum of a three-phase induction motor at 60-Hz supply. The frequency spectrum was obtained by the discrete Fourier transform (DFT) of the motor current data sampled for 10 s. The test motor with 18 rotor slots and 2 pole pairs was running at 1657.7 r/min. There are several peaks at different frequencies, each point indicating where a current harmonic is present. As shown in (1), three factors are involved in the creation of harmonics:

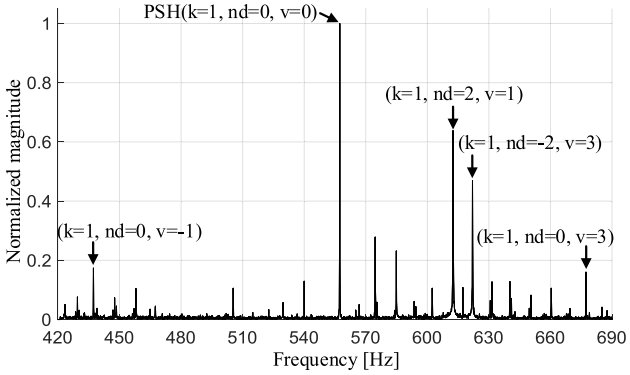

Fig. 1. Slot harmonics of the test motor at 1657.7 r/min.

rotor slots, rotor eccentricity, and stator MMF harmonics. Harmonics at different frequencies are generated by different combinations of k, n_{d}, and v. Often, as seen for the test motor, the PSH has the largest amplitude. With R and p fixed by the motor structure, the frequency of the PSH depends only on the rotor slip and the supply frequency. Thus, tracking PSH is an effective way to estimate the rotor slip

$$s = 1 - \frac{p}{R}\cdot\left(\frac{f_{\mathrm{PSH}} - f_{\mathrm{s}}}{f_{\mathrm{s}}}\right) \tag{3}$$

which typically ranges for practical induction machines between 0% and 5%. The PSH is therefore an example of a valuable harmonic that can be measured, in principle, by a nonintrusive power monitor to track machine operation and to differentiate the activity and operation of several machines on the same power service. Unfortunately, the PSH may be several orders of magnitude smaller in amplitude than the utility frequency fundamental current. It is therefore difficult to locate. This problem is exacerbated by any variations in the utility frequency, which happen frequently, and which complicates the design of a filter to reject fundamental frequency current.

III. Data Acquisition, Processing, and Filtering

To improve the detectability of rotor slot harmonics, this section introduces the architecture of a data acquisition, processing, and filtering board that can selectively and adaptively reject larger signal components in favor of much smaller harmonics. Fig. 2 shows a block diagram of the design, which provides eight-channels of simultaneously sampled data at sampling rates as high as 24 kHz. Two key features offered by the design include a zero-crossing detector for line frequency estimation and a switched capacitor (SC) notch filter with tunable center frequency. A microcontroller coordinates the operation of the SC filter and data sampling. One of the eight input channel signals is selected for the slot harmonic detection by the microcontroller using an 8:1 multiplexer.

The zero-crossing detector allows the microcontroller to detect the frequency of the dominant (for example, utility frequency) fundamental component in the chosen signal. It consists of op-amp circuits for scaling and biasing, and a hysteresis comparator depicted in Fig. 3. The front-end low-pass filter eliminates input noise that can cause undesirable

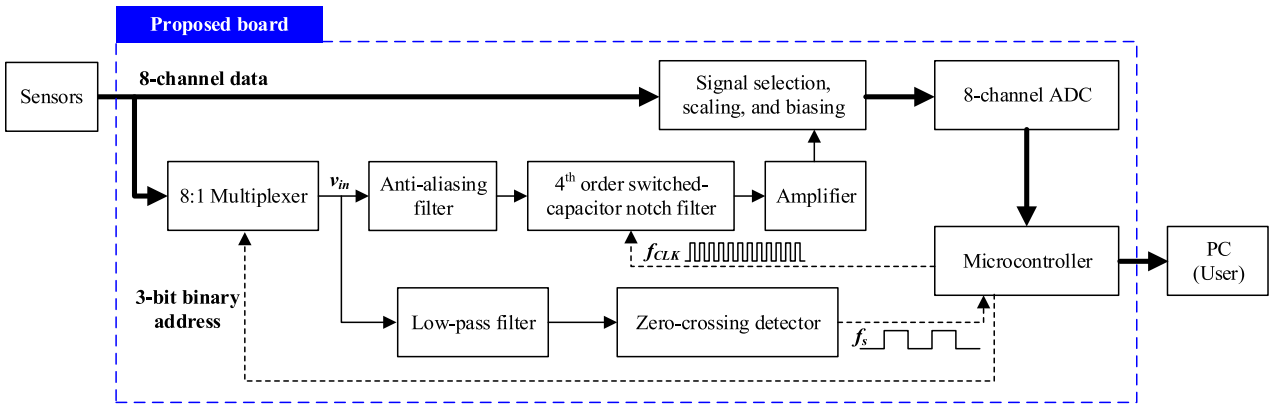

Fig. 2. Block diagram of the proposed data acquisition, processing, and filtering board.

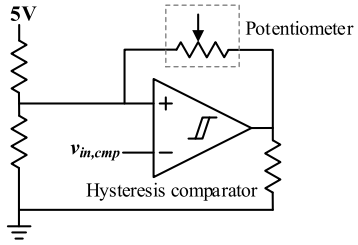

Fig. 3. Configuration of the hysteresis comparator circuit.

transitions in the comparator output and also attenuates harmonics other than the fundamental. Then, the comparator generates a pulse signal from which the microcontroller estimates the fundamental frequency of the signal. As shown in Fig. 3, a hysteresis comparator with adjustable hysteresis band helps ensure accurate zero-crossing detection with a potential phase delay that does not affect fundamental frequency estimation.

Considering that the SC notch filter is a discrete-time filter, a second-order low-pass filter is applied before the SC filter as an antialiasing filter to restrict the bandwidth of the input signal [24]. The cutoff frequency of the antialiasing filter is set to 3.1 kHz, much higher than the input frequency band of interest, allowing for a tradeoff between aliasing and bandwidth. Then, the SC notch filter is implemented with a cascade of two second-order notch filters constructed using the LTC 1060 from Linear Technology, Milpitas, CA, USA. The center frequencies are adjustable with an external clock provided by the microcontroller. The microcontroller adapts the clock frequency to follow the fundamental signal, and therefore allows the notch filter to effectively attenuate the line frequency component even if the line frequency changes.

The structure of the proposed fourth-order SC notch filter, which consists of the LTC 1060, an external clock and gain-tuning resistors, is illustrated in Fig. 4(a). The overall structure is based on a state-variable filter design with two-stage integration. Each filter block can produce various filter functions, such as lowpass, bandpass, highpass, notch, and all-pass. Here, each SC block is configured to work like a second-order filter circuit as shown in Fig. 4(b) and provide the following transfer function:

$$G(s) = H_0 \frac{s^2 + \omega_n^2}{s^2 + \frac{s\omega_n}{Q} + \omega_n^2} \tag{4}$$

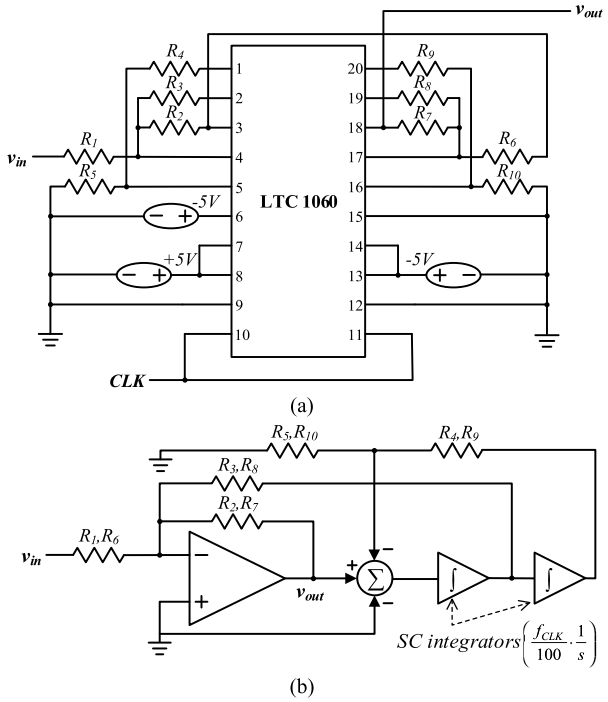

Fig. 4. (a) Configuration of the proposed SC notch filter. (b) Equivalent circuit of each filter block.

where H_0 is the filter gain when the frequency approaches zero or half the clock frequency, Q is the quality factor, and ω_n is the notch frequency. The first block is designed using R_1 to R_5, as

$$H_{0,1} = -\frac{R_2}{R_1}, \quad Q_1 = \frac{R_3}{R_2}\sqrt{\frac{R_5}{R_4 + R_5}}$$
$$\omega_{n,1} = \frac{2\pi f_{CLK}}{100}\sqrt{\frac{R_5}{R_4 + R_5}} \tag{5}$$

where f_{CLK} is the frequency of the external clock signal from the microcontroller. The ratio of the clock frequency to the notch frequency is fixed by resistance values. The second filter block is also designed with the same principle, using R_6 to R_{10}. Two filter blocks are designed to have the same frequency ratio, allowing the microcontroller to tune their

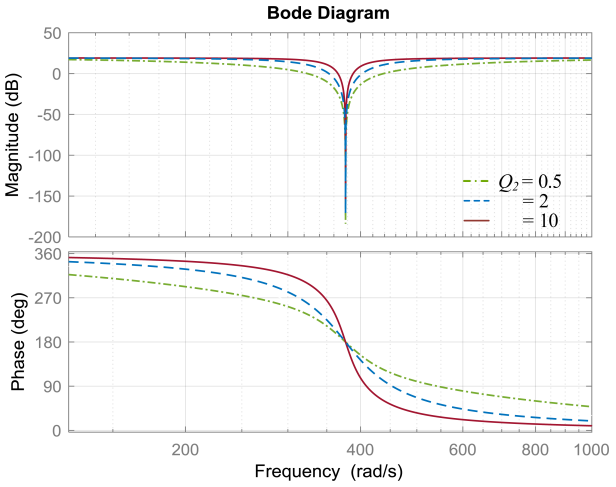

Fig. 5. Bode plot of the transfer function of the proposed fourth-order SC notch filter, with Q_1 fixed to 3.625.

cutoff frequencies to the supply frequency simultaneously. The microcontroller detects the supply frequency by capturing the timer value on every rising edge of the input pulse signal from the zero-crossing detector. Then, the clock frequency for notch filter tuning is calculated considering the frequency ratio, and finally the clock signal is generated by a pulsewidth modulator (PWM) module in the microcontroller.

The overall transfer function of the SC notch filter cascade is

$$G_{\mathrm{SC}}(s) = G_1(s) \cdot G_2(s) = H_{0,1}H_{0,2}\frac{\left(s^2+\omega_{\mathrm{n}}^2\right)\left(s^2+\omega_{\mathrm{n}}^2\right)}{\left(s^2+\frac{s\omega_{\mathrm{n}}}{Q_1}+\omega_{\mathrm{n}}^2\right)\left(s^2+\frac{s\omega_{\mathrm{n}}}{Q_2}+\omega_{\mathrm{n}}^2\right)} \tag{6}$$

where the subscript "1" and "2" stand for the first and second filter blocks, respectively. The quality factors determine the ratio of the center frequency to stopband width. In Fig. 5, the green dash-dot curve, blue-dashed curve, and red solid curve represent Bode plots of the transfer function when Q_2 is 0.5, 2, and 10, respectively, while Q_1 is fixed to 3.625. As shown in Fig. 5, for larger Q_2, the stopband is narrower. A large Q-factor is preferred for the proposed board, in which the notch filter is used to eliminate a single frequency component.

In addition to the bandwidth, the Q-factors determine the filter damping ratio. If the supply frequency varies from ω_i to ω_f at time τ, the fundamental component of a measured signal can be generally expressed with a step change

$$\begin{aligned} v_{\mathrm{in}} &= A_i \cos(\omega_i t + \phi_i) \cdot u(t) \\ &\quad + \left\{-A_i \cos(\omega_i t + \phi_i) + A_f \cos\left(\omega_f t + \phi_f\right)\right\} \cdot u(t-\tau) \end{aligned} \tag{7}$$

where A_i and A_f are the amplitudes, and ϕ_i and ϕ_f are the phases before and after time τ, respectively. As the fundamental frequency, that is the supply frequency, changes the period of the pulse train output by the zero-crossing detector changes accordingly. The microcontroller, which updates the period information on the rising edge of the input pulse, adjusts the filter clock period proportionally. Fig. 6 illustrates the

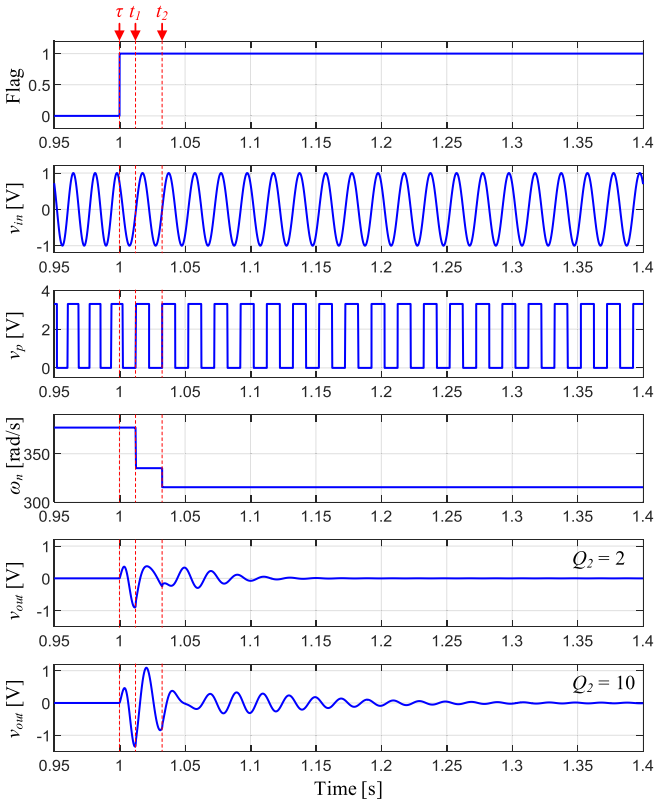

Fig. 6. Transient response of the zero-crossing detector and SC notch filter.

transition of the pulse wave, v_{p}, and notch frequency, ω_{n}, when the supply frequency changes from 60 to 50 Hz. In Fig. 6, the flag changes from 0 to 1 to show the point at which the input frequency changes. At the time τ, the supply frequency drops to 50 Hz, and the period of the pulse wave increases. The microcontroller detects the change in period on the first rising edge after time τ, occurring at time t_1. The transient period T_{t} between edges before and after τ is determined as

$$\frac{2\pi}{\max\left(\omega_i, \omega_f\right)} \leq T_{\mathrm{t}} = \frac{2\pi}{\omega_{\mathrm{t}}} \leq \frac{2\pi}{\min\left(\omega_i, \omega_f\right)} \tag{8}$$

where ω_{t} is the transient angular frequency between ω_i and ω_f. On the next rising edge at time t_2, the microcontroller obtains period information regarding the final frequency and outputs the corresponding clock signal. Thus, the center frequency of the SC notch filter changes over two steps in time as follows:

$$\omega_{\mathrm{n}} = \begin{cases} \omega_i, & (0 \leq t < t_1) \\ \omega_{\mathrm{t}}, & (t_1 \leq t < t_2) \\ \omega_f, & (t_2 \leq t). \end{cases} \tag{9}$$

As an exception, if the supply frequency changes exactly on the rising edge, the center frequency is adjusted directly from ω_i to ω_f without a transient period.

With this model, we can predict the performance of the filter. The time-domain signal in (7) can be converted to an

s-domain function by Laplace transform as

$$V_{\text{in}}(s) = L\{v_{\text{in}}\} = A_i\left[\frac{s}{s^2+\omega_i^2}\cdot\left\{\cos\phi_i - e^{-\tau s}\cos(\omega_i\tau+\phi_i)\right\} - \frac{\omega_i}{s^2+\omega_i^2}\cdot\left\{\sin\phi_i - e^{-\tau s}\sin(\omega_i\tau+\phi_i)\right\}\right] + A_f e^{-\tau s}\cdot\left[\frac{s}{s^2+\omega_f^2}\cdot\cos\left(\omega_f\tau+\phi_f\right) - \frac{\omega_f}{s^2+\omega_f^2}\cdot\sin\left(\omega_f\tau+\phi_f\right)\right] \quad (10)$$

where $L\{\}$ is the Laplace transform of the function. With (10) as a model of the input signal, the output voltage of the SC notch filter is determined as (11), as shown at the bottom of the next page in the frequency domain. In (11), C represents the amplitude of each voltage component, determined by the amplitude and frequency of the input signal and the characteristics of the SC notch filter. The subscript "c" and "s" stand for the cosine and sine components, and the subscript "τ" means that the voltage appears after time τ. This expression is applied before and after transients with discrete changes in the notch frequency, ω_{n}, resulting from supply frequency variations as in (9). The transfer function, G_{SC}, is used on the assumption that the line frequency disturbance is small. The initial value of the output voltage is redefined as the value at that point when ω_{n} changes. The output voltage has four components oscillating at different frequencies as separated by square brackets. The voltages in the first two brackets are steady sinusoidal signals with constant amplitudes. Their amplitudes are zero if the center frequency of the notch filter matches the signal frequency. When the supply frequency changes, the center frequency of the SC notch filter is tuned to the changed supply frequency at the first rising edge or the second one that follows. These sine waves exist for the time required for the notch frequency to be adjusted and not after that. Unlike them, the voltages in the last two brackets are transient sine waves with amplitudes that decay over time. As shown in Fig. 6, they appear in transients if the amplitude or frequency of the input signal changes and then diminish. The damping ratios that indicate how rapidly transient oscillations decay depend on the quality factors of two notch filter blocks

$$\zeta_1 = \frac{1}{2Q_1}, \quad \zeta_2 = \frac{1}{2Q_2}. \quad (12)$$

The smaller the Q-factor, the greater the damping ratio and the faster the transient oscillations are attenuated. The bottom two waveforms in Fig. 6 show the output voltages for different Q_2 values. Q_1 was fixed to 3.625 as in Fig. 5. As expected, the transient oscillation damped quickly within about 150 ms when Q_2 was small, while the oscillation damped relatively slowly over about 400 ms when Q_2 was large. Thus, the Q-factor of the proposed notch filter is designed to be large enough to sharply drop the gain of the center frequency, but not too large to dampen transient oscillations in a short time.

The resistance values that determine the gains and Q-factors of the two notch filter blocks in Fig. 4 are designed as in Table I. The orange curve in Fig. 7 shows the designed gains of the SC notch filter. It is designed to have a sharp drop in gain near the center frequency to accurately remove only the line frequency component. It is also intended to amplify the gain in the high frequency range by about 18 dB, that is about eight times, to detect relatively small slot harmonics. The purple dots in Fig. 7 represent the experimentally measured gains of the practically implemented notch filter. The designed and measured gains are compared in the wide frequency range on the logarithmic scale in Fig. 7(a) and in the frequency range of interest around 60 Hz in Fig. 7(b). The implemented notch filter provides a gain very close to that designed.

Fig. 8 shows the experimental results to verify the transient notch filtering performance, which automatically detects then removes the fundamental component. In the experiment, the supply frequency dropped from 60 to 50 Hz and then increased back to 60 Hz. The A-phase motor current signal is used for the fundamental frequency detection. The output voltage of the A-phase current sensor was input to the zero-crossing detector and notch filter. As shown in the second waveform of Fig. 8(a), both the frequency and amplitude of the motor currents changed in a transient state of frequency change and then converged to the new values. Fig. 8(b) shows magnified waveforms around time τ when the frequency drops. As shown in the third waveform, the fundamental frequency

TABLE I
DESIGN VALUES OF RESISTORS IN TWO NOTCH FILTER BLOCKS

Symbol	Value (kΩ)	Symbol	Value (kΩ)
R_1	19.6	R_6	6.2
R_2	31.6	R_7	34.8
R_3	162	R_8	332
R_4	3.48	R_9	3.48
R_5	3.48	R_{10}	3.48

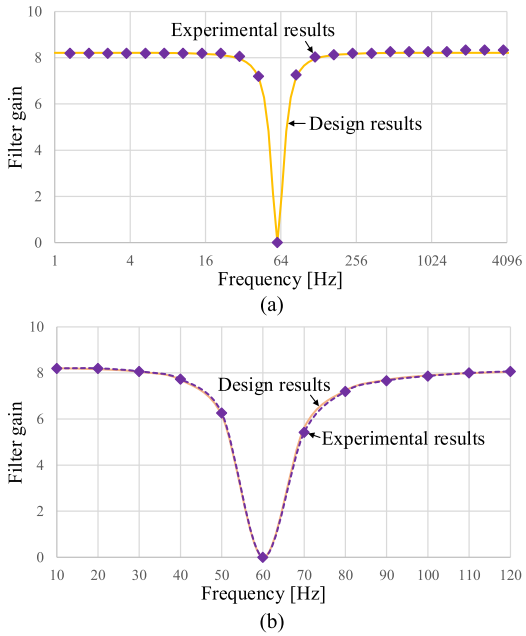

Fig. 7. Comparison of designed and experimentally measured filter gains. (a) In the wide frequency range on the logarithmic scale. (b) In the frequency range of interest around 60 Hz.

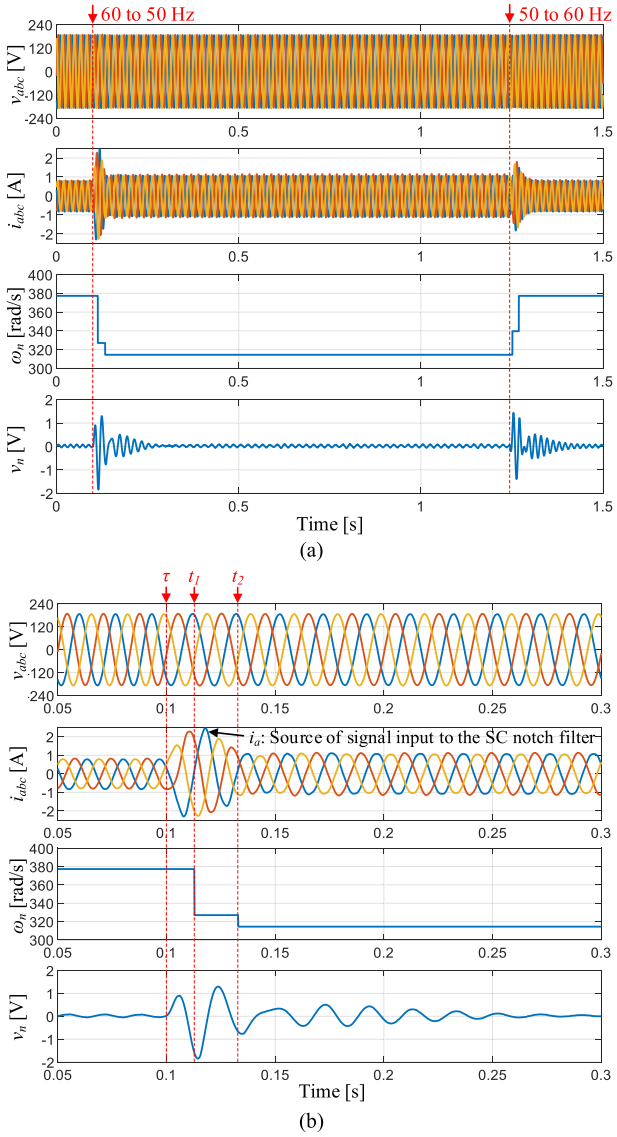

Fig. 8. (a) Transient performance of the zero-crossing detector and SC notch filter as the supply frequency changes from 60 to 50 to 60 Hz. (b) Magnified waveforms when the supply frequency drops from 60 to 50 Hz.

of the A-phase current was detected on its rising edge, and the center frequency of the notch filter was automatically tuned. As a result, the fundamental component was successfully attenuated within 0.2 s when the frequency suddenly either dropped or increased.

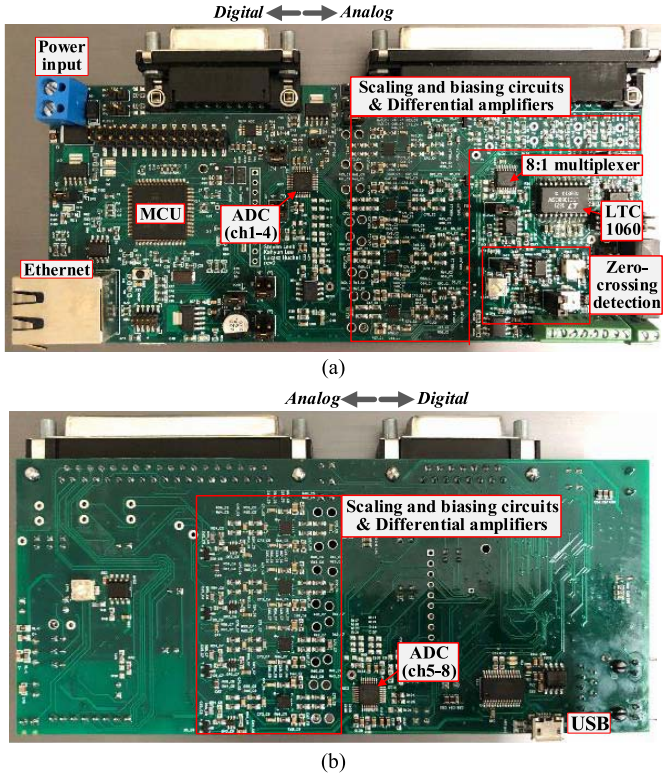

Fig. 9. (a) Top and (b) bottom sides of the prototype acquisition board.

A total of eight signals are selected for analog-to-digital conversion, based on user configuration. They are scaled and biased to fit the input range of the ADC, an ADS131A04 from Texas Instruments, Dallas, TX, USA, which allows simultaneous sampling of four channels at high data rates. Two ADCs are daisy chained to perform simultaneous sampling of all eight channels of data. Serial digital data are passed to the microcontroller using the Serial Peripheral Interface (SPI) connection at 16-bit resolution and 8-kHz sampling rate for our experiments. The prototype board allows the user to receive data via Ethernet, USB, UART, or I2C. In our experiments, we recover six channels of raw utility three-phase voltages and currents, one channel for the estimated utility or fundamental frequency, and one channel for a filtered current waveform with the fundamental removed. This filtered waveform can be inspected for subtle harmonics, as described in the speed sensing demonstration in Section IV.

$$V_n(s) = G_{\mathrm{SC}}(s)\cdot V_{\mathrm{in}}(s) = \left[\frac{s}{s^2+\omega_i^2}\cdot\left(C_{ic}+e^{-\tau s}C_{ic,\tau}\right)+\frac{\omega_i}{s^2+\omega_i^2}\cdot\left(C_{is}+e^{-\tau s}C_{is,\tau}\right)\right]+\left[\frac{se^{-\tau s}}{s^2+\omega_f^2}\cdot C_{fc}+\frac{\omega_f e^{-\tau s}}{s^2+\omega_f^2}\cdot C_{fs}\right]$$
$$+\left[\frac{\left(s+\frac{\omega_{\mathrm{n}}}{2Q_1}\right)\left(C_{1c}+e^{-\tau s}C_{1c,\tau}\right)}{\left(s+\frac{\omega_{\mathrm{n}}}{2Q_1}\right)^2+k_1^2\omega_{\mathrm{n}}^2}+\frac{k_1\omega_{\mathrm{n}}\left(C_{1s}+e^{-\tau s}C_{1s,\tau}\right)}{\left(s+\frac{\omega_{\mathrm{n}}}{2Q_1}\right)^2+k_1^2\omega_{\mathrm{n}}^2}\right]$$
$$+\left[\frac{\left(s+\frac{\omega_{\mathrm{n}}}{2Q_2}\right)\left(C_{2c}+e^{-\tau s}C_{2c,\tau}\right)}{\left(s+\frac{\omega_{\mathrm{n}}}{2Q_2}\right)^2+k_2^2\omega_{\mathrm{n}}^2}+\frac{k_2\omega_{\mathrm{n}}\left(C_{2s}+e^{-\tau s}C_{2s,\tau}\right)}{\left(s+\frac{\omega_{\mathrm{n}}}{2Q_2}\right)^2+k_2^2\omega_{\mathrm{n}}^2}\cdot C_{2s}\right],\quad k_x=\sqrt{1-\frac{1}{4Q_x^2}}\ (x=1,2) \tag{11}$$

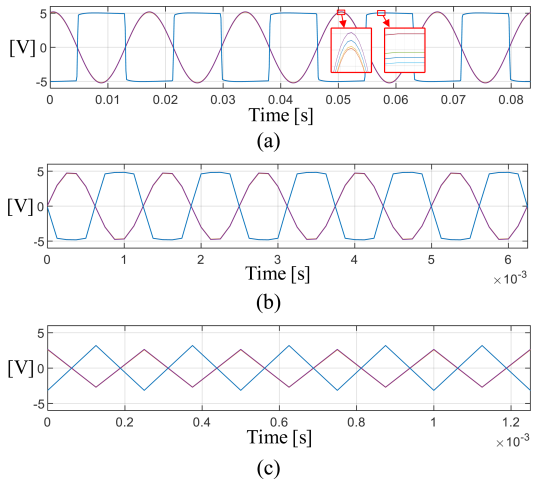

Fig. 10. Data transferred by the proposed board. (a) 60 Hz. (b) 800 Hz. (c) 4 kHz.

Fig. 9(a) and (b) shows the prototype acquisition system, with different functional regions of the board identified in the images. Fig. 10 shows example data transferred to a desktop computer via Ethernet by simultaneously sampling eight-channel data at 8 kHz with the prototype. Sine waves were input to the first four channels, and pulse waves were input to the 5th to 8th channels. The base frequencies were increased from 60 to 800 Hz, then 4000 Hz in Fig. 10(a)–(c), respectively.

IV. Principle Slot Harmonic Tracking

This section demonstrates the real-world performance of the prototype board by tracking the slot harmonics of an induction machine operated with changing utility frequencies. There are two steps for detecting the PSH through spectral analysis of the current waveforms. The first step is to set the finite length of a realistic frequency span where the PSH will be located, and the second is to find the frequency of the PSH within the window. With two steps, an aggregate current waveform containing the line currents of several motors or loads can be analyzed to find the "fingerprint" PSH of a particular motor of interest. The PSH frequency window is determined from either a field observation of the motor of interest or design details like the number of rotor bars in the machine. This information may be available for motors in "designed" industrial plants like refineries or manufacturing facilities.

For typical efficiency induction motors, it is possible to confine the window in which the PSH is located with the practical assumption that the motor is operated at less than 5% slip. Under this assumption, the PSH can be reliably detected in a finite window and the slip can be uniquely estimated using (3), as described in [1]. The frequency window presented in [1] assumes that the line frequency is 60 Hz and has a fixed length of 120 Hz, which is vulnerable to changes in supply frequency.

To reliably detect the PSH regardless of supply frequency variations, this section proposes a window with a length of $2f_s$

$$f_{\omega 1} = f_s(R/p - 1) \le f \le f_{\omega 2} = f_s(R/p + 1) \qquad (13)$$

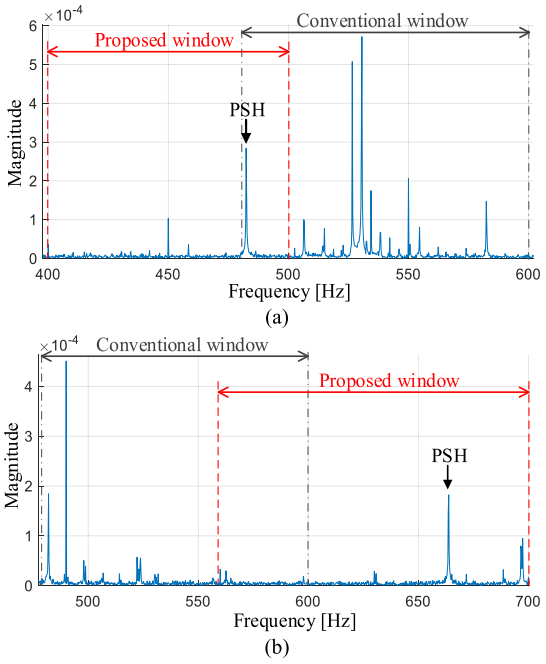

Fig. 11. Comparison between the conventional and proposed windows for PSH tracking. (a) $f_s = 50$ Hz. (b) $f_s = 70$ Hz.

where $f_{\omega 1}$ and $f_{\omega 2}$ represent the frequencies at which the PSH detection window begins and ends, respectively. The window with a length of $2f_s$ is effective in the slip range

$$0 \le s \le \frac{2p}{R}. \qquad (14)$$

This covers the practical 5% slip range for motors with up to 40 rotor slots per pole pair. Our test motor is one such example.

Fig. 11(a) and (b) shows the current spectra when the motor is running at about 4% slip with a 50-Hz supply and at about 5% slip with a 70-Hz supply, respectively. The conventional window in [1] is fixed at 480–600 Hz for the test motor with 18 slots and 2 pole pairs, regardless of the supply frequency. Such a window includes harmonics other than the PSH when the supply frequency is 50 Hz, making the PSH no longer the most dominant harmonic as shown in Fig. 11(a). Also, with a 70-Hz supply, the PSH is located outside the window as shown in Fig. 11(b), making it impossible to detect the PSH. In contrast, the proposed method employs a flexible window as (13), with a 400–500-Hz window for 50 Hz, and a 560–700-Hz window for 70 Hz. For both cases, the proposed window includes the PSH as the most dominant harmonic.

After the window is set according to (13), the next step is to find the frequency of PSH through spectral analysis within the window. The simplest way is to choose the frequency with the largest amplitude in the window. However, this method limits the resolution of the frequency and associated speed estimate to the size of DFT frequency bins, which is inversely proportional to the data acquisition time for the data window. We seek to identify the speed with as quickly an acquired data window as possible. Fig. 12 shows the DFT spectrum of motor current near the PSH, at 10- and 0.1-s sampling durations. The vertical black-dotted lines indicate where the

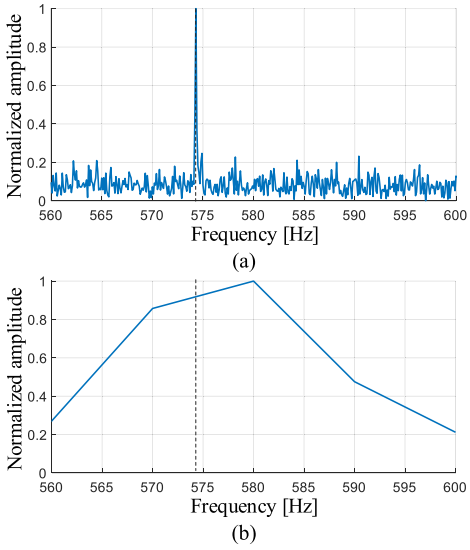

Fig. 12. Motor current spectrum for different sampling times. (a) 10 s. (b) 0.1 s.

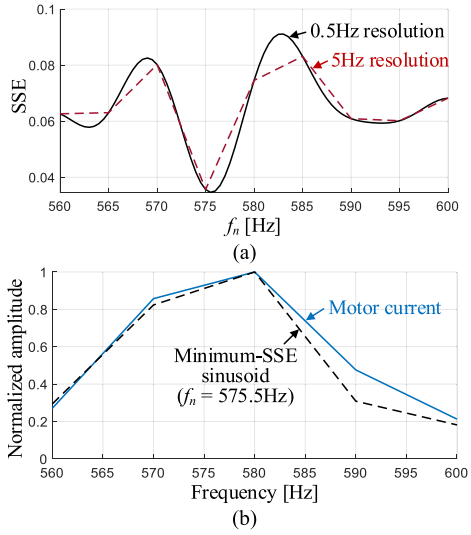

Fig. 13. (a) SSEs according to the frequency of the pure sinusoid. (b) DFT spectrum of the motor current and minimum-SSE sinusoid.

PSH is located. As shown in Fig. 12(a), a long sampling interval allows the PSH's energy to be concentrated in a specific frequency bin, making it possible to accurately detect the PSH's frequency. However, long intervals are not preferred for estimation of motor speed, which is likely to change over time. Shortening the sampling intervals may improve dynamic response and reduce computation burden. However, it causes the PSH's energy to spread wider across the frequency bins, as shown in Fig. 12(b). This increases the error of the PSH frequency estimate. Choosing the largest amplitude with 0.1-s data sampling results in more than 1% error.

Assuming that other harmonics near the PSH are negligibly small, the accuracy of frequency estimation can be improved by finding the best-fit sinusoid with the DFT spectrum closest to the motor current. The criterion for best-fit is set to minimize the sum of squared errors (SSEs) near the peak as

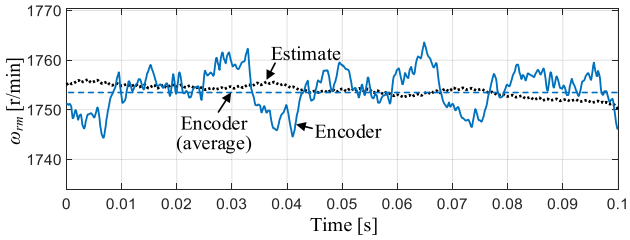

Fig. 14. Steady-state waveforms of the measured and estimated speeds.

in [1]

$$\mathrm{SSE}(f_n) = \sum_{k=k_1}^{k_2} |C(f_n) \cdot X_{s,k}(f_n) - X_{i,k}|^2$$

$$C(f_n) = \sqrt{\frac{\sum_{k=k_1}^{k_2} |X_{i,k}|^2}{\sum_{k=k_1}^{k_2} |X_{s,k}(f_n)|^2}}, \quad f_n = f_1 + \frac{n}{N_f}(f_2 - f_1) \tag{15}$$

where $X_{i,k}$ is the DFT spectrum of the notch-filtered motor current, $X_{s,k}$ is the DFT spectrum of the sine wave with frequency f_n, and C is the scale factor. f_1 and f_2 are the beginning and end of the frequency range where the squared error is summed near the peak, and k_1 and k_2 are the corresponding frequency indices. The larger N_f, the higher the frequency resolution to find the best-fit sinusoid. Applying an optimization algorithm targeting the current DFT of Fig. 12(b) yields the result shown in Fig. 13. Fig. 13(a) shows the SSE according to the sinusoid frequency, f_n, when f_1 is 560 Hz, f_2 is 600 Hz, and N_f is 80 or 8. Even with 0.1 s of data acquisition resulting in a 10-Hz DFT resolution, increasing N_f can find the best-fit frequency with less error. The minimum-SSE frequency found at 0.5-Hz resolution is 575.5 Hz with 0.2% error as shown in Fig. 13(b). This is one-fifth of the error seen when looking for the peak frequency directly from the DFT result.

From the supply frequency detected by the prototype board and the estimated PSH frequency, motor speed is estimated as

$$\hat{\omega}_{rm} = \frac{2\pi}{p}(1 - \hat{s})\hat{f}_s = \frac{2\pi}{R}\left(\hat{f}_{\mathrm{PSH}} - \hat{f}_s\right). \tag{16}$$

V. Speed Estimation Performance

Given the PSH frequency, we can track motor speed. The test motor has 18 rotor slots and 2 pole pairs and was loaded by a dynamometer. The prototype board sent eight-channel data to the user's computer, including the detected supply frequency, and a filtered current waveform with the fundamental removed. The motor speed was then estimated in real time with PSH frequency tracking. The frequency values and speed estimate were updated in synchronization with 8-kHz data sampling. The supply frequency was detected by a 120-MHZ, 32-bit timer in the microcontroller at each rising edge of the input pulse. Given a frequency range of 0–120 Hz, the supply frequency value had a 1.8-MHz resolution. On the other hand, the PSH frequency tracked by the spectral analysis of the

TABLE II

SPEED ESTIMATES AT DIFFERENT SAMPLING TIMES AND TRACKING METHODS

ω_{rm} (r/min)	Sampling time (s)	PSH tracking method	f_{PSH} (Hz)	ω_{rm} est. (r/min)	Error (%)
1764.11	10	Peak	589.2	1764	-0.006
	1	Peak	589	1763.33	-0.044
	0.1	Peak	590	1766.67	0.145
	0.1	Min. SSE (0.1Hz)	589.4	1764.67	0.032
1775.16	10	Peak	592.5	1775	-0.009
	1	Peak	592	1773.33	-0.103
	0.1	Peak	590	1766.67	-0.478
	0.1	Min. SSE (0.1Hz)	593.6	1778.67	0.198
1787.48	10	Peak	596.2	1787.33	-0.008
	1	Peak	596	1786.67	-0.045
	0.1	Peak	600	1800	0.7
	0.1	Min. SSE (0.1Hz)	596.6	1788.67	0.067

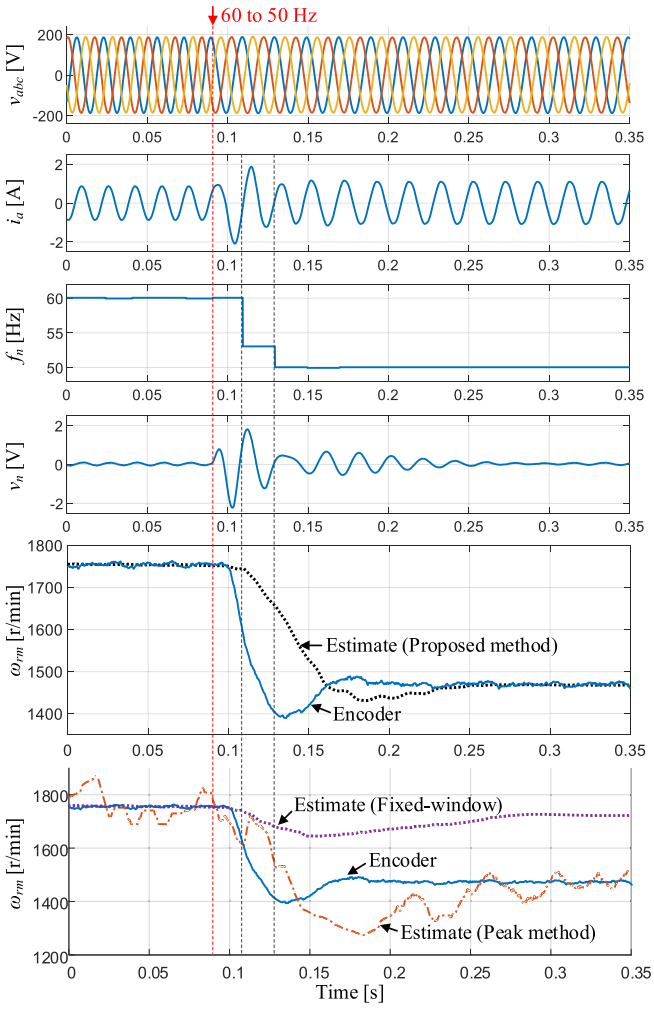

Fig. 15. Transient performance of the proposed and conventional speed estimators when the supply frequency is changed from 60 to 50 Hz.

current waveform had an accuracy depending on the data acquisition time and tracking method.

Table II shows the steady-state speed estimation results for different sampling times and tracking methods. Sampling times of 10, 1, and 0.1 s were applied at three different

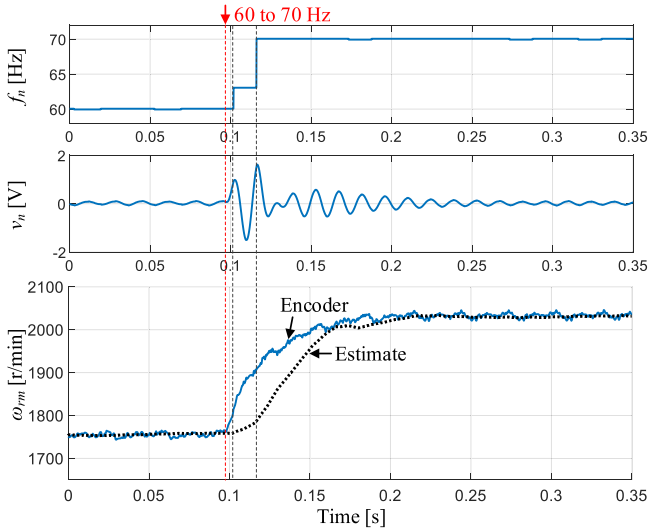

Fig. 16. Transient performance of the proposed speed estimator when the supply frequency is changed from 60 to 70 Hz.

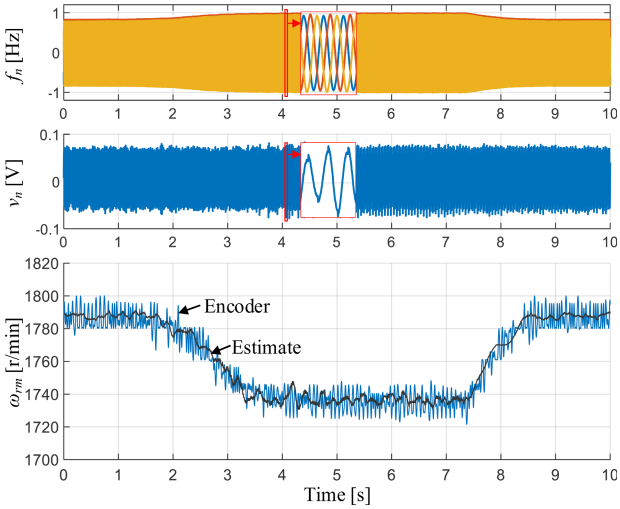

Fig. 17. Transient performance of the proposed speed estimator when the load torque from the dynamometer is changed.

rotor speeds. The minimum SSE method applied to improve the accuracy of PSH frequency detection was compared to the conventional peak method of simply picking the peak frequency within the window. As the data acquisition time shortened, the accuracy of PSH frequency detected by the peak method deteriorated significantly. In contrast, the minimum SSE method allowed precise frequency detection even with short data acquisition of 0.1 s. Compared to the peak method, it achieved the same accuracy with one-tenth the sampling time. In the following experiments, the PSH frequency was tracked at 0.1-Hz accuracy with 0.1-s data acquisition and minimum SSE method.

Fig. 14 shows the steady-state speed waveforms measured with the optical encoder and the speed estimate by the proposed algorithm when the motor was running at about 2.6% slip with a 60-Hz supply. The proposed method of instantaneously estimating the average speed from the data

for the previous 0.1 s accurately estimated the average speed with an error within 0.1%. Using previously sampled data entailed limitations for tracking high-frequency speed ripple. Still, the speed estimator provided improved dynamic response over existing methods that required long data acquisition for comparable accuracy.

To evaluate the dynamic performance of the proposed speed estimator, the supply frequency or load torque was changed during speed estimation. In Figs. 15 and 16, the supply frequency was changed from 60 to 50 and 70 Hz, respectively. To discover important patterns in motor speed, a 10-ms moving average filter for noise reduction was applied to speed measurements and estimates. In Fig. 15, the supply frequency was reduced in step at the red-dotted line, and then the frequency change was detected at the rising edges of the A-phase current indicated by black-dotted lines, so the center frequency of the notch filter was adapted. The SC notch filter attenuated the fundamental component in less than 0.2 s. The speed estimate, applying the proposed slot harmonic tracking method to the notch-filtered current, quickly tracked rotor speed changes with a delay of about 0.1 s and effectively converged to the new speeds. For comparison, existing methods were considered in the bottom waveforms. To evaluate the effectiveness of the flexible frequency window reflecting the detected supply frequency in real time, a PSH tracking method using a fixed window as in [1] was applied as indicated by the purple dotted curve. The speed estimated by this method could not follow the motor speed from the moment the supply frequency dropped. In addition, the peak method was applied to detect the PSH frequency in the orange dash-dotted curve instead of the minimum SSE method. The peak method caused large errors in speed estimation due to the low accuracy of frequency detection. In contrast, the proposed approach allowed the speed estimate to quickly follow the motor speed with a delay of approximately 0.05 s even when the supply frequency was increased to 70 Hz, as depicted in Fig. 16.

Fig. 17 illustrates the speed estimation when the rotor speed was changed by load variations. The dynamometer stepped load torque from zero to approximately two-third of a Newton-meter and back to zero. Connected to a 60-Hz supply, the motor runs at about 0.7% slip, slows down to about 3.5% slip, and then speeds up again. The proposed speed estimator accurately tracked such speed changes.

VI. Conclusion

This article has demonstrated a custom data acquisition system tailored to the needs of nonintrusive power monitoring on the ac utility. The board can be applied in any application where a wide range of interesting harmonics are "buried" in a large fundamental frequency waveform. The transient performance and settling time of the board's tracking capability can be predicted with analytical tools described in this article. The performance of the system has been demonstrated for rotor slot harmonic tracking and speed estimation. The combination of the prototype design and the tracking algorithm has been proved experimentally to estimate the speed quickly and accurately in transient as well as steady state.

Acknowledgment

The authors gratefully acknowledge the support of The Grainger Foundation, the Exelon-MITei agreement, and the Office of Naval Research NEPTUNE program.

References

[1] U. A. Orji *et al.*, "Non-intrusive induction motor speed detection," *IET Electric Power Appl.*, vol. 9, no. 5, pp. 388–396, May 2015.
[2] S. Qin, Z. Huang, and X. Wang, "Optical angular encoder installation error measurement and calibration by ring laser gyroscope," *IEEE Trans. Instrum. Meas.*, vol. 59, no. 3, pp. 506–511, Mar. 2010.
[3] S.-T. Wu, J.-Y. Chen, and S.-H. Wu, "A rotary encoder with an eccentrically mounted ring magnet," *IEEE Trans. Instrum. Meas.*, vol. 63, no. 8, pp. 1907–1915, Aug. 2014.
[4] R. M. Kennel, "Encoders for simultaneous sensing of position and speed in electrical drives with digital control," *IEEE Trans. Ind. Appl.*, vol. 43, no. 6, pp. 1572–1577, Nov./Dec. 2007.
[5] M. Sahraoui, A. J. M. Cardoso, K. Yahia, and A. Ghoggal, "The use of the modified Prony's method for rotor speed estimation in squirrel-cage induction motors," *IEEE Trans. Ind. Appl.*, vol. 57, no. 3, pp. 2194–2202, May/Jun. 2016.
[6] Z. Gao, L. Turner, R. S. Colby, and B. Leprettre, "A frequency demodulation approach to induction motor speed detection," *IEEE Trans. Ind. Appl.*, vol. 47, no. 4, pp. 1632–1642, Jul. 2011.
[7] X. Song, B. Han, and K. Wang, "Sensorless drive of high-speed BLDC motors based on virtual third-harmonic back EMF and high-precision compensation," *IEEE Trans. Power Electron.*, vol. 34, no. 9, pp. 8787–8796, Sep. 2019.
[8] S. Foti, A. Testa, S. De Caro, T. Scimone, and M. Pulvirenti, "Rotor flux position correction and parameters estimation on sensorless multiple induction motors drives," *IEEE Trans. Ind. Appl.*, vol. 55, no. 4, pp. 3759–3769, Jul. 2019.
[9] K. Wang, R. D. Lorenz, and N. A. Baloch, "Improvement of back-EMF self-sensing for induction machines when using deadbeat-direct torque and flux control," *IEEE Trans. Ind. Appl.*, vol. 53, no. 5, pp. 4569–4578, Sep. 2017.
[10] X. Song, J. Fang, B. Han, and S. Zheng, "Adaptive compensation method for high-speed surface PMSM sensorless drives of EMF-based position estimation error," *IEEE Trans. Power Electron.*, vol. 31, no. 2, pp. 1438–1449, Feb. 2016.
[11] W. Sun, J. Gao, Y. Yu, G. Wang, and D. Xu, "Robustness improvement of speed estimation in speed-sensorless induction motor drives," *IEEE Trans. Ind. Appl.*, vol. 52, no. 3, pp. 2525–2536, May 2016.
[12] O. Keysan and H. B. Ertan, "Real-time speed and position estimation using rotor slot harmonics," *IEEE Trans. Ind. Informat.*, vol. 9, no. 2, pp. 899–908, May 2013.
[13] M. K. Metwaly, N. I. Elkalashy, M. S. Zaky, and T. M. Wolbank, "Slotting saliency extraction for sensorless torque control of standard induction machines," *IEEE Trans. Energy Convers.*, vol. 33, no. 1, pp. 68–77, Mar. 2018.
[14] M. Aiello, A. Cataliotti, and S. Nuccio, "An induction motor speed measurement method based on current harmonic analysis with the Chirp-Z transform," *IEEE Trans. Instrum. Meas.*, vol. 54, no. 5, pp. 1811–1819, Oct. 2005.
[15] Z. Gao, T. G. Habetler, R. G. Harley, and R. S. Colby, "A sensorless rotor temperature estimator for induction machines based on a current harmonic spectral estimation scheme," *IEEE Trans. Ind. Electron.*, vol. 55, no. 1, pp. 407–416, Jan. 2008.
[16] K. D. Hurst and T. G. Habetler, "A comparison of spectrum estimation techniques for sensorless speed detection in induction machines," *IEEE Trans. Ind. Appl.*, vol. 33, no. 4, pp. 898–905, Jul./Aug. 1997.
[17] M. Ishida and K. Iwata, "A new slip frequncy detector of an induction motor utilizing rotor slot harmonics," *IEEE Trans. Ind. Appl.*, vol. IA-20, no. 3, pp. 575–582, May 1984.
[18] D. S. Zinger, F. Profumo, T. A. Lipo, and D. W. Novotny, "A direct field-oriented controller for induction motor drives using tapped stator windings," *IEEE Trans. Power Electron.*, vol. 5, no. 4, pp. 446–453, Oct. 1990.
[19] A. Ferrah *et al.*, "A speed identifier for induction motor drives using real-time adaptive digital filtering," *IEEE Trans. Ind. Appl.*, vol. 34, no. 1, pp. 156–162, Jan./Feb. 1998.
[20] A. Ferrah, K. J. Bradley, and G. M. Asher, "An FFT-based novel approach to noninvasive speed measurement in induction motor drives," *IEEE Trans. Instrum. Meas.*, vol. 41, no. 6, pp. 797–802, Dec. 1992.

[21] P. L. Jansen and R. D. Lorenz, "Transducerless position and velocity estimation in induction and salient AC machines," *IEEE Trans. Ind. Appl.*, vol. 31, no. 2, pp. 240–247, Mar./Apr. 1995.
[22] K. D. Hurst and T. G. Habetler, "Sensorless speed measurement using current harmonic spectral estimation in induction machine drives," *IEEE Trans. Power Electron.*, vol. 11, no. 1, pp. 66–73, Jan. 1996.
[23] M. El Hachemi Benbouzid, "A review of induction motors signature analysis as a medium for faults detection," *IEEE Trans. Ind. Electron.*, vol. 47, no. 5, pp. 984–993, Oct. 2000.
[24] A. V. Oppenheim, R. W. Schafer, and J. R. Buck, *Discrete-Time Signal Processing*, 2nd ed. Upper Saddle River, NJ, USA: Prentice-Hall, 1999, pp. 185–187.

Kahyun Lee (Member, IEEE) received the B.S. and Ph.D. degrees in electrical engineering from Seoul National University, Seoul, South Korea, in 2013 and 2018, respectively.

She is currently a Post-Doctoral Associate with the Research Laboratory of Electronics, Massachusetts Institute of Technology, Cambridge, MA, USA. Her research interests include electric machine control, signal processing, and condition monitoring.

Lukasz Huchel (Student Member, IEEE) received the B.Sc. degree in electrical power engineering from the Silesian University of Technology, Gliwice, Poland, in 2013, and the M.Sc. degree from the Department of Electrical Engineering and Computer Science, Masdar Institute of Science and Technology, Abu Dhabi, United Arab Emirates (UAE). He is currently pursuing the Ph.D. degree in EECS with the Massachusetts Institute of Technology, Cambridge, MA, USA.

His research interests include the development of signal processing algorithms, as well as the hardware and software solutions for condition monitoring and diagnostics.

Daisy H. Green (Graduate Student Member, IEEE) received the B.S. degree from the University of Hawai'i at Mānoa, Honolulu, HI, USA, in 2015, and the M.S. degree in electrical engineering from the Massachusetts Institute of Technology, Cambridge, MA, USA, in 2018, where she is currently pursuing the Ph.D. degree.

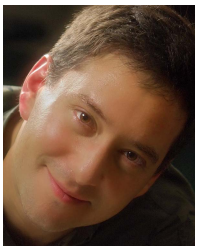

Steven B. Leeb (Fellow, IEEE) received the Ph.D. degree from the Massachusetts Institute of Technology (MIT), Cambridge, MA, USA, in 1993.

He has served as a Commissioned Officer with the USAF Reserves, GA, USA, and has been a member of the MIT Faculty, Department of Electrical Engineering and Computer Science, MIT, since 1993. He also holds a joint appointment with the Department of Mechanical Engineering, MIT. He has authored or coauthored over 200 publications and holds 20 U.S. patents in the fields of electromechanics and power electronics.